Nuclear Science and Techniques (2026) 37:10
https://doi.org/10.1007/s41365-025-01802-4

Feasibility study of a LYSO-SiPM-based prototype for hybrid Compton and PET imaging

Hai-Hao Wang[1,2] · Yu-Cun Hou[1,2] · Jian-Lang Hua[1,2] · Zi-Quan Yuan[1,2] · Chen-Xi Li[1,2] · Run-Ze Liao[1,2] · Jian-Yong Jiang[1,2]

Received: 13 May 2024 / Revised: 26 August 2024 / Accepted: 31 August 2024 / Published online: 7 December 2025
© The Author(s), under exclusive licence to China Science Publishing & Media Ltd. (Science Press), Shanghai Institute of Applied Physics, the Chinese Academy of Sciences, Chinese Nuclear Society 2025

Abstract

We present a prototype for hybrid Compton and positron emission tomography (PET) imaging aimed at enhancing data utilization and enabling concurrent imaging of multiple radiopharmaceuticals. The prototype comprises two detectors that utilize LYSO-SiPM and were available in our laboratory. One detector consists of a 50 × 50 array of LYSO crystals, each measuring 0.9 mm × 0.9 mm × 10 mm with 1 mm pitches, whereas the other detector comprises a 25 × 25 array of LYSO crystals, each measuring 1.9 mm × 1.9 mm × 10 mm with 2 mm pitches. These detectors are mounted on a rotational stage, which enables them to function as either a Compton camera or a PET detector pair. The 64-channel signals from the SiPMs of each detector are processed through a capacitive multiplexing circuit to yield four position-weighted outputs. Distinct energy windows were used to discriminate Compton events from PET events. Energy resolution and energy-channel relationships were calibrated via multiple sources. The measured average energy resolutions (full widths at half maximum, FWHMs) for the detectors at 511 keV were 17.5% and 15.2%, respectively. The initial experimental results indicate an angular resolution (FWHM) of 8.6° for the system in Compton imaging mode. A V-shaped tube injected with ^{18}F solution was clearly reconstructed, which further verified the imaging capabilities of the system in Compton imaging mode. The results of simulation and experimental imaging studies show that the system can detect tumors as small as 1 mm in diameter when working in PET imaging mode. Mouse bone PET imaging was successfully conducted, with the results matching well with the corresponding CT images. This technology holds great potential for advancing the development of physiological function modalities.

Keywords Positron emission tomography (PET) · Compton camera · Image reconstruction

1 Introduction

Positron emission tomography (PET) is a sophisticated non-invasive medical imaging modality that is predicated upon positron emission radionuclide labeling and facilitates the quantification of cellular metabolism within bodily tissues [1–6]. Central to PET imaging is the use of positron emission radiopharmaceuticals, notably ^{18}F-deoxyglucose (^{18}F-FDG), which functions as a glucose analog. Upon administration into the patient's body, FDG is distributed in accordance with physiological and pathological processes. Given its structural absence of a hydroxyl group at the C-2 position, FDG cannot be further metabolized, which results in its entrapment within tumor cells in proportion to glucose utilization rates, thereby enabling increased radioactive deposition within tumor sites [7, 8]. The positrons emitted from decay undergo annihilation radiation with electrons, which results in a pair of gamma photons with an energy of 511 keV being emitted in opposite directions, as depicted in Fig. 1a. The coincidence detection of these gamma photons provides insight into tracer transport, metabolism, and binding. PET has garnered attention for applications related

This work was supported by the National Natural Science Foundation of China (No. 12105018), the Beijing Nova Program (Nos. Z211100002121129 and 20230484413), and the Beijing Normal University Start-up Grant (No. 312232104).

✉ Jian-Yong Jiang
jianyong@bnu.edu.cn

[1] School of Physics and Astronomy, Beijing Normal University, Beijing 100875, China

[2] Key Laboratory of Beam Technology of the Ministry of Education, Beijing Normal University, Beijing 100875, China

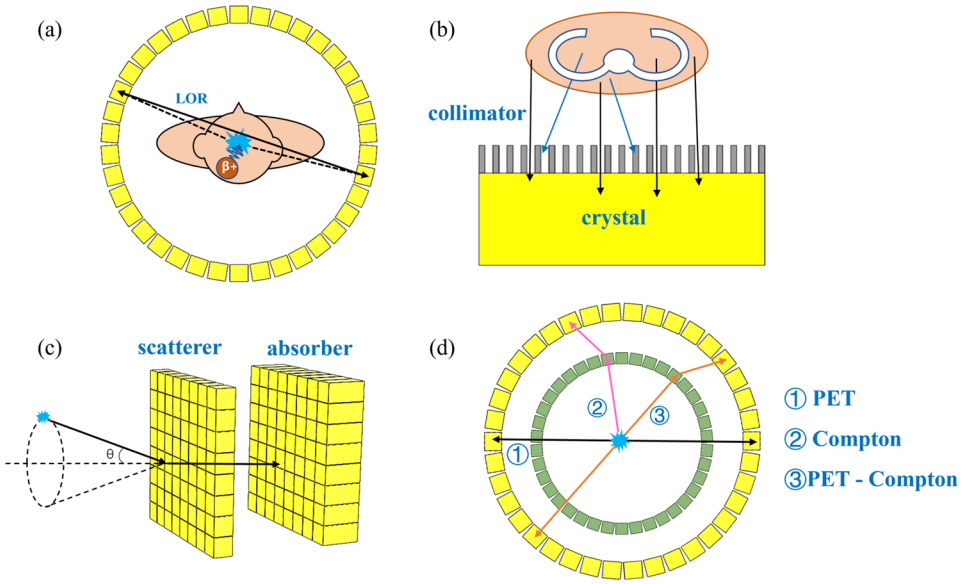

Fig. 1 (Color online) **a** Imaging principle of PET, where the black solid line represents the line of response determined by a pair of gamma photons and the dashed line represents the actual flight path of the gamma photon pair; **b** SPECT, where photons from specific directions are collected through mechanical collimation; **c** a Compton camera, which calculates cones of potential source locations based on the Compton scattering kinematics; and **d** the Compton/PET hybrid imaging system, which allows for the detection of three different types of coincidence events and imaging in three modes

to tumor diagnosis, radiopharmaceutical development, neurological disorders, and biodynamic modeling [9–14]. Critical to PET imaging are positron emission radionuclides [15, 16], such as ^{18}F, ^{11}C, ^{13}N, and ^{15}O. Moreover, certain single-photon emission nuclides, such as ^{99m}Tc, ^{67}Ga, ^{111}In, and ^{123}I, prove indispensable in elucidating physiological metabolic processes [17–21]. Nevertheless, the predominant emission of gamma rays renders these nuclides incompatible with PET systems. As illustrated in Fig. 1b, single-photon emission computed tomography (SPECT) addresses this limitation and enables the imaging of such radioisotopes via mechanical collimation [22–24].

The integration of PET/SPECT dual-tracer imaging systems has broadened the application of nuclear medicine in medical diagnosis, where it augments clinical and preclinical research approaches [25–30]. Studies have underscored the enhanced diagnostic accuracy afforded by PET/SPECT for certain malignancies, such as thyroid cancer [31–33]. Simultaneous imaging with ^{131}I and ^{18}F-FDG demonstrates divergent patterns in thyroid tissue accumulation, which mitigates the risk of misdiagnosis, particularly in assessing therapeutic efficacy [34–37]. Nonetheless, concurrent PET and SPECT image acquisition poses challenges, including potential interference between imaging modalities and compromised sensitivity of PET due to collimators within the SPECT system, alongside the introduction of unwanted background signals into SPECT images through the interactions of 511 keV photons [38].

With advancements in detector technology, the exploration of Compton cameras for various applications, particularly in medical imaging, is receiving increasing attention [39–43]. As illustrated in Fig. 1c, Compton cameras typically comprise two detector layers: a scatterer and an absorber. Gamma rays scattered in the scatterer and then absorbed in the absorber create cones of potential source locations. Combining these overlapping cones from multiple sequences produces an image of the source distribution. Notably, Compton cameras can detect gamma rays that span from tens of keV to several MeV and reconstruct the three-dimensional distribution of radiation sources [44–49]. By imaging gamma photons of various energies without mechanical collimators, a Compton/PET hybrid imaging system provides a wider field of view than does PET/SPECT, thereby resulting in improved system sensitivity and overcoming the challenges inherent in simultaneous PET and SPECT image acquisition [50–53].

As illustrated in Fig. 1d, a Compton/PET hybrid imaging system discriminates coincidence events based on photon energy and utilizes both Compton and photoelectric events for image reconstruction. Commercial PET systems exhibit relatively low sensitivity of approximately 1% [54]. A key contributing factor lies in Compton scattering inducing changes in the photon flight direction, which introduces additional noise during image reconstruction. Consequently, a considerable proportion of Compton scattering events are excluded during reconstruction. Regrettably, this process entails discarding valuable information encapsulated in Compton events. Leveraging Compton events to obtain valuable information could bolster system sensitivity [55, 56]. PET events, which occur when neither photon undergoes scattering, are employed directly for PET imaging. Compton events, which occur when one photon scatters and all its energy is ultimately deposited in the detectors, are utilized for Compton imaging. In instances where one photon scatters and the other does not, $\beta^+ - \gamma$ triple coincidence detection is conducted to integrate the direction information of the scattered photon into image reconstruction [51].

Certain β^+ decays are accompanied by single gamma photons, which increases noise in PET scans. Through $\beta^+ - \gamma$ triple coincidence, the intersection of PET-derived LORs with Compton cone imaged regions furnishes precise source localization. The 3D Compton cone complements traditional LOR-based PET approaches by translating scattering events into orientation information, thereby augmenting system sensitivity and the image signal-to-noise ratio [57, 58]. In 2017, Yamaya et al. pioneered the whole gamma imaging (WGI) prototype [59, 60]. In 2020, they achieved experimental imaging in PET, single-photon and triple-gamma modes [51, 61]. Other radioisotopes, such as ^{44m}Sc, ^{48}V, ^{86}Y, ^{94}Tc, and ^{152}Tb, are anticipated for use in positron–gamma imaging [62, 63]. This optimization markedly enhances the data utilization efficiency, captures more effective information within a single scan, and consequently enhances the overall imaging accuracy [64].

The ability of Compton/PET hybrid imaging systems to detect triple coincidence of $\beta^+ - \gamma$ events with multitracer imaging heralds a new era in dual-tracer PET detection methods. For example, in cardiovascular investigations, the simultaneous administration of ^{82}Rb-chloride and ^{18}F-FDG can be used to assess both the metabolic rate and perfusion kinetics [65]. However, when two different positron radiopharmaceuticals are administered simultaneously or sequentially, the detector records information from both nuclides as 511 keV gamma photons in dual-tracer PET. Consequently, the detector is unable to distinguish between the two signals, which poses a significant obstacle to dual-tracer PET image reconstruction. Historically, obtaining images of the double tracer has been complex and has relied on dynamic modeling, arterial input functions, deep learning and longitudinal PET [66–73]. Given that some positron-emitting drugs emit a single photon during β^+ decay, the Compton/PET hybrid imaging system can identify each tracer for independent imaging through $\beta^+ - \gamma$ triple coincidence detection. The ability of this technology to facilitate multitracer imaging is critical for advancing physiological function research and holds great potential for future development.

In addition to positron–gamma imaging, a hybrid Compton/PET system enables multinuclide imaging. In nuclear medicine, timely detection of cancer and real-time monitoring of recurrence in vivo present significant challenges, particularly in the early diagnosis of tumors via PET and in distinguishing between benign and malignant lesions [74, 75]. To characterize cancer and surrounding tissues fully, improve diagnostic accuracy, and tailor the best treatment strategy, the use of multiple nuclides to obtain detailed information is imperative [76–79]. In 2020, the Compton/PET hybrid imaging system proposed by Shimazoe et al. successfully imaged ^{18}F-FDG and ^{111}In [50]. In 2021, the research group subsequently achieved simultaneous imaging of dual nuclides in a mixture of ^{131}I and ^{18}F-FDG [52].

Considering these advantages of hybrid Compton/PET systems, we built a prototype for hybrid Compton and PET imaging based on lutetium–yttrium oxyorthosilicate (LYSO) scintillator crystals and silicon photomultipliers (SiPMs). Characterization of the system and assessment of its imaging performance in both PET and Compton imaging modes were conducted. Custom reconstruction software was developed for both the Compton camera and PET via the list-mode maximum likelihood estimation maximization (MLEM) method, which was executed across multiple graphics processing units (GPUs). Imaging experiments with various phantoms and small mice were carried out to evaluate the effectiveness of the hybrid prototype.

2 Materials and methods

2.1 System design

We constructed a Compton/PET hybrid imaging system from two existing detectors available in the laboratory. One detector is composed of a LYSO array of 50×50 crystals, each measuring 0.9 mm × 0.9 mm × 10 mm with a pitch of 1mm, whereas the other detector is composed of a LYSO array of 25×25 crystals, each measuring 1.9 mm × 1.9 mm × 10 mm with a pitch of 2 mm. The LYSO crystals were polished and optically isolated via 0.1-mm-thick $BaSO_4$ reflectors, and the outside of the crystal array was also covered with $BaSO_4$ reflectors. Both detectors are directly read out by an 8×8 SiPM (SenSL MicroFC-60035) array. The dimensions of the 8×8 SiPM array are 50.79 mm × 50.79 mm, with each pixel measuring 6 mm × 6 mm. Preliminary experiments have shown that flood images of two crystal arrays can be decoded relatively efficiently via a 4 mm thick light guide [80]. Therefore, in this study, optical glue of 4 mm thickness was used for the coupling between the crystal arrays and SiPM arrays. The two detectors were mounted on a rotational stage to form either a Compton camera or a PET detector pair (not simultaneously in this preliminary study). When the detectors are arranged one in front of the other, the system operates in Compton imaging mode, with the 50×50 array detector working as the scatterer and the other as the absorber, as shown in Fig. 2a. Conversely, when the two detectors are positioned face to face, the system operates in PET imaging mode, as shown in Fig. 2b. For the Compton camera, the center-to-center distance of the two detectors for this evaluation study was set to 102 mm. For PET imaging, the two detectors on the rotational stage can independently be rotated to any desired angle and direction to mimic full-ring PET imaging. The maximum face-to-face distance between the two detectors is 137 mm, which means that the PET has a radial field of view of 137 mm and an axial field of view of 50 mm.

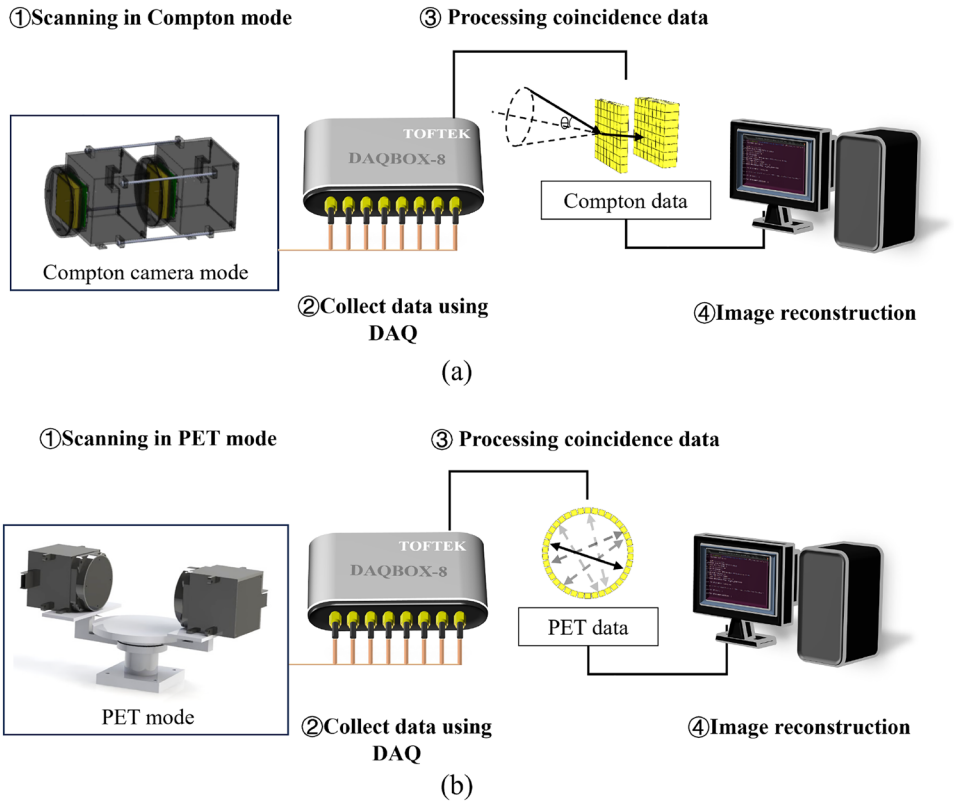

Fig. 2 (Color online) The detection process of the proposed Compton/PET hybrid imaging prototype for **a** Compton imaging mode and **b** PET imaging mode. After the DAQ collects the raw data, Compton and PET coincidence events are differentiated based on time and energy. These events are then used separately for Compton and PET image reconstruction

The scintillation photons generated by the interaction of gamma rays in the LYSO crystal diffuse through the light guide and are transmitted to the 8×8 SiPM array. The encoding circuit feeds the 64-channel signals from the SiPMs of each detector into a capacitive multiplexing circuit to reduce the number of signals to 4 position-weighted outputs. A custom data acquisition card (DAQ) manufactured by TOFTEK (Wuxi, China) recorded 8-channel output signals from both detectors. Data acquisition was carried out in the single mode. The four-channel signals of each detector were summed and compared with the high and low thresholds. The time when the signal crossed the lower threshold was recorded (with a time unit of 20 ns), and the interaction position and energy information of a single event were obtained via Anger logic. In both Compton and PET imaging modes, data coincidence was performed between single-photon events from the two detectors, and the coincidence time window was set to 20 ns (limited by the sampling speed of the DAQ). The energy window for PET events was set to 460 keV to 560 keV. The Compton events were also filtered in the reconstruction process. For ^{18}F, an energy window of $0-200$ keV was applied to the scattering energy to eliminate the backscattering effect, and an energy window of $460-560$ keVwas applied to the sum of the scattering energy and the absorption energy. For ^{60}Co, the two energy windows used for imaging 1.17 MeV gamma rays were $0-600$ keV and $1055-1290$ keV.

2.2 Detector evaluation

To extract position and energy information from the raw data, a flood image was measured by each detector, and the energy–channel relationship of each individual crystal was established. The detectors were characterized via the setup shown in Fig. 3. The detectors and source were housed within a shading box, and the 4-channel readout signals from each detector were extracted via SMA cables and transmitted to the DAQ. Two flood images were generated with 75 million single-photon events each when irradiated by a ^{22}Na source. Detector lookup tables were generated by running a custom automatic peak finding code followed by manual

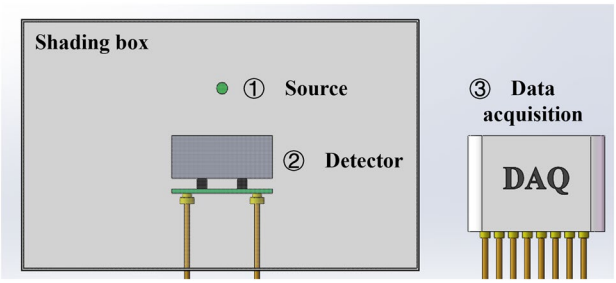

Fig. 3 (Color online) The detectors and source were housed within a shaded box, and the 4-channel readout signals from each detector were transmitted to the DAQ

correction. These lookup tables were used to delineate the regions that correspond to each individual crystal within the flood image. The energy calibration of each single crystal was performed with three radionuclides of different energies, ^{99m}Tc, ^{22}Na and ^{176}Lu. The position of the photopeak was determined by Gaussian fitting of the energy spectrum. The average energy resolution of the 511 keV photoelectric peak was computed for all discernible crystals within the detector.

2.3 Monte carlo simulation

The overall imaging performance of the proposed prototype Compton/PET hybrid imaging system was evaluated via GATE simulation [81]. To simplify the simulation, evaluations of the PET component and the Compton camera component were conducted separately.

The configuration of the Compton camera mirrors that of the actual Compton camera that we constructed, with its geometry depicted in Fig. 4a, in which the red dot represents the point source. The angular resolution (FWHM) of the Compton camera was assessed by imaging a ^{18}F point source positioned 2 cm away from the scatterer center. The detection efficiency of the prototype was evaluated by employing an ideal ^{18}F point source that was moved among six different positions from –50 mm to 50 mm in the radial direction, with a step size of 1 mm. The absolute detection efficiency at each position was subsequently calculated.

As in the actual design, the configuration of the PET in the simulation also comprised two detectors, as shown in Fig. 4b, with the red cylinder representing the phantom. These detectors were rotated at various angles to mimic full-ring PET imaging. The imaging performance of the PET system was evaluated by using the small animal NEMA PET phantom and the Derenzo phantom. The small animal NEMA phantom is composed predominantly of a cylinder that measures 30 mm in diameter and length and contains two cold rods, each with a diameter of 8 mm. Additionally, it features five rod sources with diameters that range from 1 mm to 5 mm, which are distributed as illustrated in Fig. 5a–b. As shown in Fig. 5c, the Derenzo phantom is composed of six groups of rod sources with diameters of 0.8, 1.0, 1.25, 1.5, 2.0 and 2.5 mm, respectively. The center-to-center spacing between every two sources is greater than twice the source diameter . Both phantoms were injected with ^{18}F solution with a total initial activity of 3.7 MBq. Data were acquired from twelve angles, with rotations taking place every 15°, and scanning was conducted for 10 min at each angle.

2.4 Experimental study

For the Compton camera, the imaging capability was evaluated by using a ^{60}Co source positioned approximately 2 cm away from the scatterer center. The source was subsequently relocated to five additional positions, as shown in Fig. 6a–b. V-shaped tubing filled with ^{18}F was also imaged to evaluate the imaging capability of the Compton camera when it was irradiated by a distributed source. The imaging study setup depicted in Fig. 6c illustrates a V-shaped tube filled with the ^{18}F solution.

For PET, we performed imaging studies with the small animal NEMA PET phantom (PET/NEMA-SA/P), as shown in Fig. 7a. The experimental setup for phantom imaging is illustrated in Fig. 7b. The main part of the cylindrical phantom is composed of a fillable cylindrical cavity with a diameter and length of 30 mm, and one end is sealed by a cover. Two cold-filled chambers are provided on the cover, as shown in Fig. 5a. Both chambers are hollow cylinders with a length of 15 mm and an internal diameter of 8 mm (an external diameter of 10 mm and a wall thickness of 1 mm). The remaining 20 mm is the solid part, and there

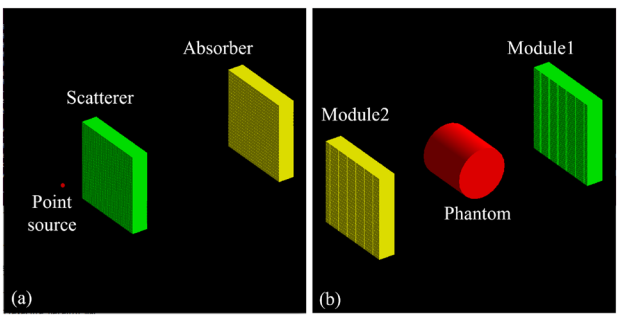

Fig. 4 (Color online) Geometry of the Compton/PET hybrid imaging system in the Monte Carlo simulation. **a** Compton imaging mode, with the red dot representing the point source. **b** PET imaging mode, with the red cylinder representing the phantom

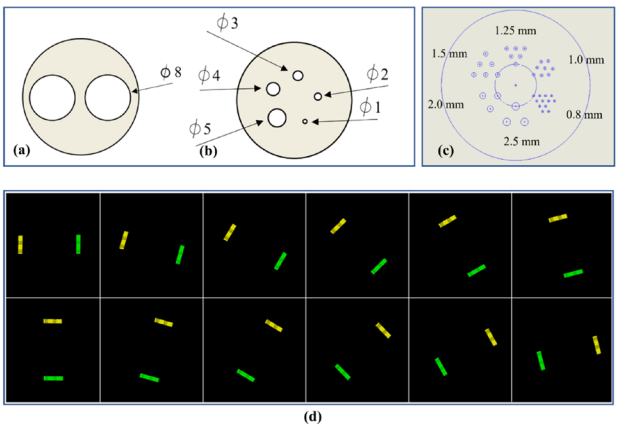

Fig. 5 (Color online) **a**–**b** Distributions of hot and cold rods, respectively, in the small animal NEMA PET phantom, **c** size and distribution of tumors in the Derenzo phantom, and **d** 12 data acquisition angles of the prototype in PET imaging mode

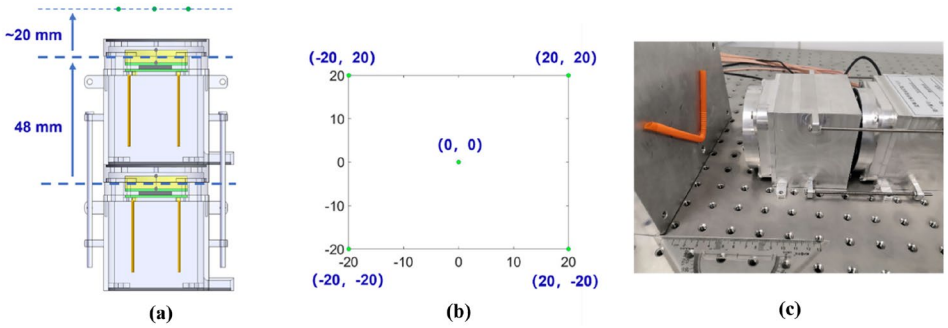

Fig. 6 (Color online) **a** Side view of the Compton camera, **b** the 5 different locations for point source imaging, and **c** the V-shaped tube that contained ^{18}F solution for Compton imaging, which was placed 5 cm away from the scatterer center

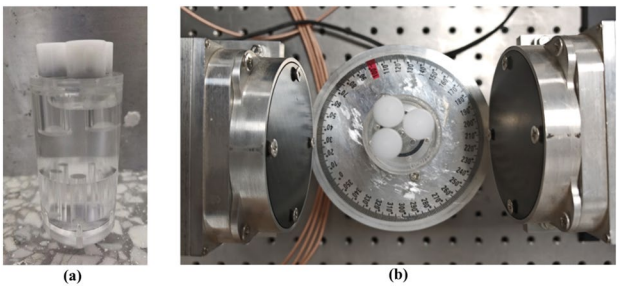

Fig. 7 (Color online) **a** Small animal NEMA phantom and **b** experimental setup for NEMA phantom imaging. The phantom was placed at the center of the rotational stage, and the two detectors were rotated to collect data from 12 different angles. At every angle, the two detectors were kept face to face

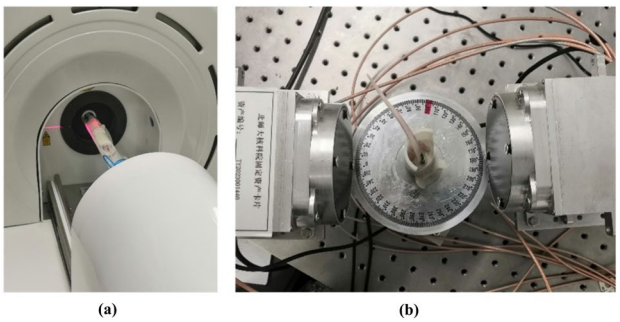

Fig. 8 (Color online) **a** CT scan of a mouse obtained using an Inviscan Imaging Systems PET/CT scanner. **b** Experimental setup for mouse imaging. Each mouse was placed at the center of the rotational stage, and the two detectors were rotated to collect data from 12 different angles. At every angle, the two detectors were kept face to face

are 5 fillable hollow rods with diameters of 1, 2, 3, 4 and 5 mm distributed 7 mm away from the center of the circle. The diameters and distribution of the 5 rods are shown in Fig. 5b. The cylindrical phantom was filled with 3.7 MBq of ^{18}F solution. The two cold rods within the main section of the phantom were nonradioactive, whereas the remaining part contained five rods that simulated tumors. The detector was rotated by 15° sequentially to collect data from 12 different angles, and data were acquired at the first angle for 10 min. At every angle, the two detectors were kept face to face to minimize the parallax error. Since the half-life of ^{18}F is approximately 2 h, the acquisition time should be appropriately extended during the scanning process to account for the influence of radioactive decay that results from scanning at various angles.

To further evaluate the imaging capabilities of the PET prototype, a mouse imaging study was conducted. A 20.8 g mouse was injected with 322.2 μCi of ^{18}F-labeled fluoride solution. Prior to PET scanning, the mouse underwent CT scanning via an Inviscan Imaging Systems PET/CT scanner, as shown in Fig. 8a. PET scanning commenced one hour after drug injection, during which data from a total of 12 angles, as shown in Fig. 5d, were collected, with an acquisition time of 5 min at the first angle. The experimental setup for the mouse imaging study is illustrated in Fig. 8b. Owing to the limited axial length of the system, whole-body imaging of the mouse within one axial field of view was not feasible. Therefore, skeletal imaging was restricted from the mouse brain to the chest. Finally, the PET and CT images were manually registered and superimposed.

2.5 Image reconstruction under both imaging modes

In this study, custom image reconstruction software for the Compton camera was developed. The software operates on multiple graphics processing units (GPUs) and is based on the list-mode maximum likelihood expectation maximization (MLEM) method [82]. The system matrix used in this study was derived based on Geant4 simulations. This involved systematically scanning a point source throughout the imaging volume, which allowed for the capture of the system's sensitivity, specifically in Compton imaging mode. The reconstructed images comprised $100 \times 100 \times 50$ voxels, with each voxel measuring 1.0 mm × 1.0 mm × 1.0 mm. The full width at half maximum (FWHM) of the distribution of the angular resolution measure (ARM) is applied to justify

the angular resolution of the Compton camera. The ARM for one coincidence event is computed as follows:

$$\mathrm{ARM} = \theta_{\mathrm{E}} - \theta_{\mathrm{G}}, \tag{1}$$

where θ_{E} represents the scattering angle calculated from the energy information from the data point via Compton scattering kinematics and where θ_{G} is calculated from the position information from the data point and the source position. The absolute detection efficiency of a Compton camera is defined by the following formula:

$$\eta = \frac{n}{N} \times 100\%, \tag{2}$$

where n represents the number of effective coincidence events obtained according to the time window and energy window in a single imaging process and N represents the total number of photons emitted by the radioactive source.

A versatile PET image reconstruction framework was also developed to accommodate various crystal sizes and spatial placements, thus supporting asymmetric PET geometric image reconstruction [83]. The software, which is also based on the list-mode MLEM algorithm, dynamically computes the system matrix on-the-fly [84, 85] and utilizes multiple GPUs for improved speed [86, 87]. This framework enables accurate and flexible PET image reconstruction tailored to the requirements of the hybrid prototype. The images were reconstructed via prompt events within a 3D rectilinear space that consisted of $200 \times 200 \times 200$ voxels, where each voxel measured 0.5 mm × 0.5 mm × 0.5 mm. A simplified version of component-based normalization, which considers both geometric effects and individual crystal efficiency, was implemented. Random and scatter corrections were not applied during the 3D image reconstruction process.

3 Results

3.1 Detector evaluation

We obtained a flood image for each detector by irradiating the whole detector with a ^{22}Na source in single mode, as shown in Fig. 9a and b. Owing to the absorption of most scintillation photons at the edge pixels of the crystal array by the coating on the side and the subsequent loss of scintillation photons at the edge following penetration of the 4mm light guide, two or three sets of crystals appear indistinct. Figure 9c and d show the profiles along the red line of each set of crystals along the reimage. For the 50×50 crystal array, 44×44 crystals can be identified from the flood image. For the 25×25 crystal array, 23×23 crystals can be identified. The average peak-to-valley ratios along the red line in Fig. 9a and b for the two flood images were 1.26±0.25 and 1.81±0.41, respectively. ^{99m}Tc, ^{22}Na and ^{176}Lu sources were used for energy calibration. The energies used for calibration were 140 keV, 511 keV, 597 keV [88, 89] and 1275 keV. The energy spectrum of a single crystal is shown in Fig. 10. The data of the photoelectric peak are selected for Gaussian fitting, and the energy calibration

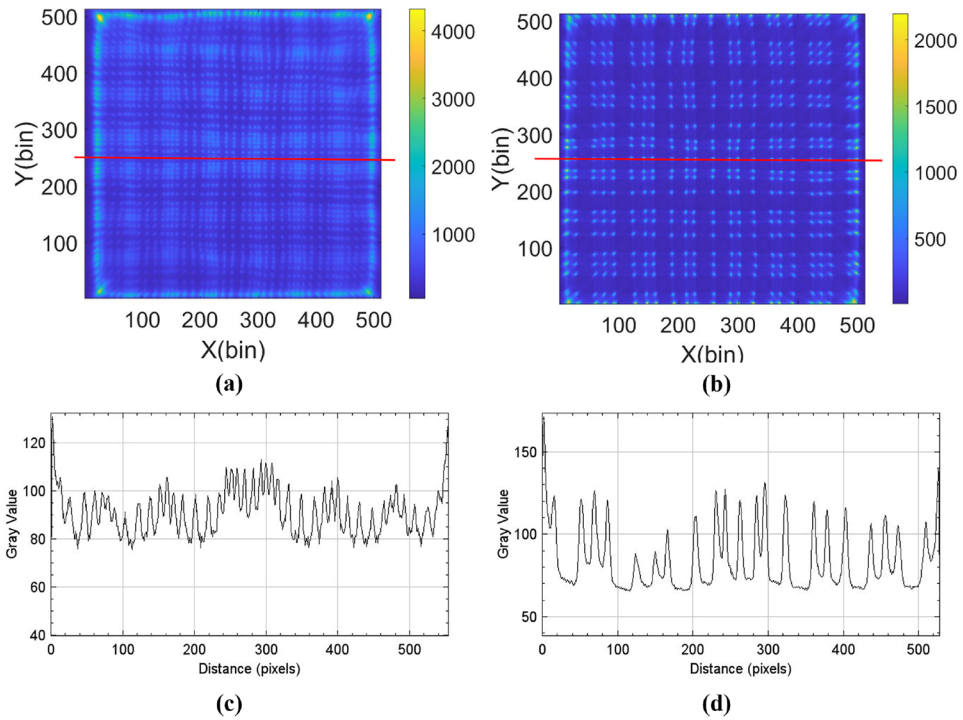

Fig. 9 (Color online) Flood images of the **a** scatterer and **b** absorber when irradiated by a ^{22}Na point source and **c** and **d** line profiles along the red line in the flood images in (a) and (b), respectively

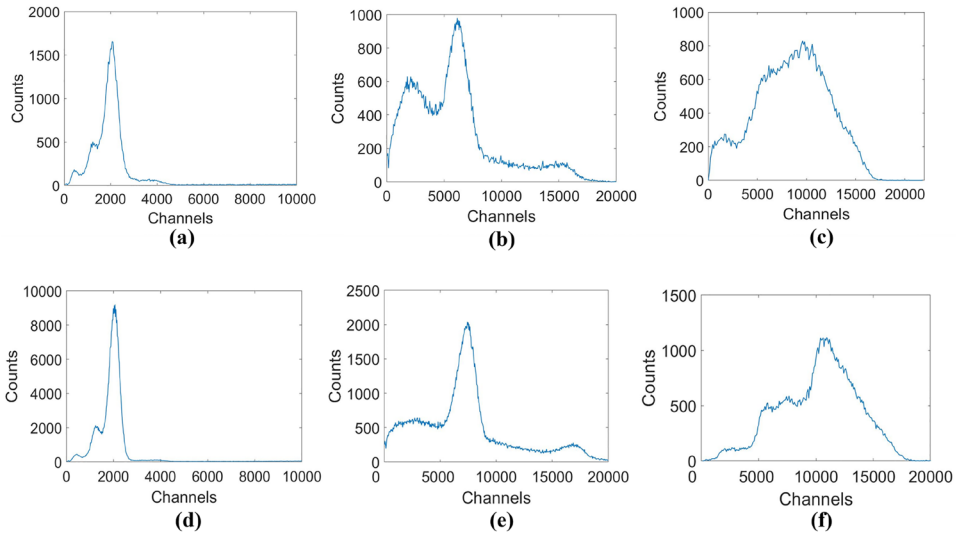

Fig. 10 (Color online) Energy spectra of the ^{99m}Tc, ^{22}Na and ^{176}Lu sources for a representative crystal in the **a**–**c** scatterer and **d**–**f** absorber

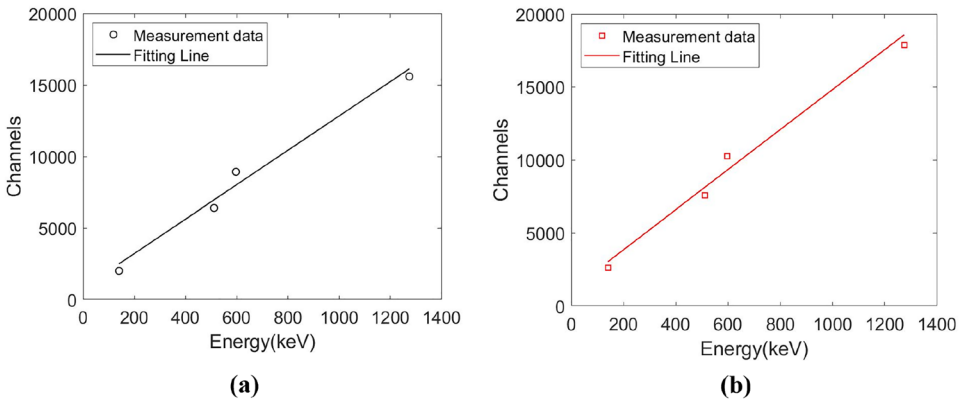

Fig. 11 (Color online) The measured energy–channel relationship of a representative crystal in the **a** scatterer and **b** absorber

curve of each individual crystal is obtained. Figure 11 shows the energy–channel relationship of a single representative crystal from the two detector modules. The average energy resolutions (FWHMs) of the scatterer and absorber were 17.5% and 15.2%, respectively, for gamma photons with an energy of 511 keV.

3.2 Monte carlo simulation

The ^{18}F point source was placed at (−20,20,0) mm with a distance of 2 cm from the scatterer center. Figure 12a shows the simulation results without consideration of the energy resolution, where the FWHM of the ARM was determined mainly by geometric factors to be approximately 3.51°. The simulation results obtained when the energy resolution of the detectors was set according to the actual measurements, namely, 17.5%@ 511 keV for the scatterer and 15.2%@ 511 keV for the absorber, are shown in Fig. 12b, where the FWHM of the ARM is approximately 7.80°. Figure 13 shows the distribution of the detection efficiency after the energy window was set.

Reconstructed images of the small animal NEMA phantom scanned by the PET prototype are shown in Fig. 14, and the data from all 12 sampling angles were used for image generation. The reconstructed images revealed that the cold rods could be well identified by the system. The hot rod sources with diameters that ranged from 1 mm to 5 mm were all clearly identified.

To further evaluate the resolving power of the PET prototype, the Derenzo phantom was simulated, and the results are shown in Fig. 15. The reconstructed image in Fig. 15a shows that the system could identify radioactive sources with a diameter of 1 mm but could not effectively identify sources with a diameter of 0.8 mm. Figure 15b shows the line profile of three rod sources with a diameter of 1 mm. The average peak-to-valley ratio is 1.63.

3.3 Experimental study

For the Compton imaging mode, the images reconstructed experimentally via the MLEM reconstruction algorithms are shown in Fig. 16 when the ^{60}Co source was subsequently

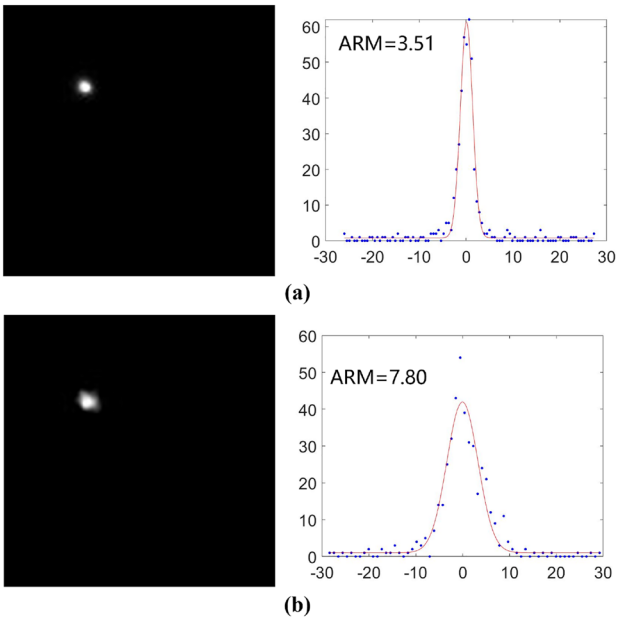

Fig. 12 (Color online) Reconstructed Compton image and ARM distribution of **a** the ^{18}F point source without considering the energy resolution and **b** the ^{18}F point source with energy resolutions of 17.5% @ 511 keV and 15.2% @ 511 keV for the scatterer and absorber, respectively

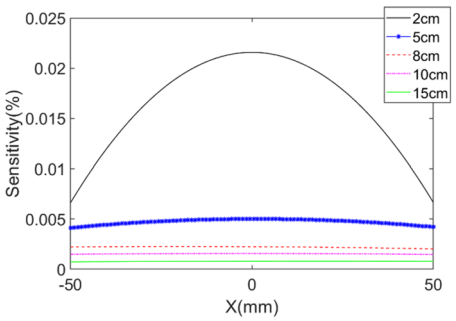

Fig. 13 (Color online) Detection efficiency of the prototype as a function of the source position in the radial direction. The different colors of the curves represent different distances from the source to the scatterer center

Fig. 14 (Color online) PET simulation results for the small animal NEMA phantom for cold rods, a uniform distribution and five rod sources

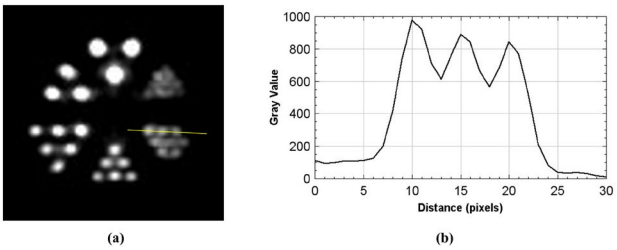

Fig. 15 (Color online) **a** PET image of the Derenzo phantom from the simulation and **b** line profile of three sources with a diameter of 1 mm along the yellow line

placed at five different locations. The ARM distribution of the experimental data is also presented in Fig. 16. The average FWHM of the ARM was approximately 8.6° when the source was 2 cm away from the scatterer center. An image of the V-shaped phantom was obtained and is shown in Fig. 17. Via a simple filtered back-projection method, the Compton camera clearly reconstructed the V-shaped phantom.

The reconstructed images of the small animal NEMA phantom in PET imaging mode are shown in Fig. 18a. Data from the 12 angles were applied. The cold rods and lesion areas were successfully identified. Additionally, five groups of rod sources that ranged from 1 to 5 mm in diameter were also clearly distinguished. Figure 18b displays the line profile of the uniform region, with a mean pixel value of 9.62 and a standard deviation of 0.42.

The mouse bone structure can be distinctly identified with ^{18}F labeling, as illustrated in Fig. 19a–c, which displays PET/CT images of three slices that depict the mouse rib, arm, and head. PET images were manually registered and superimposed with CT images. The results demonstrate a high level of consistency between the PET images and the bone images obtained via CT.

4 Discussion

In this study, we developed a Compton/PET hybrid imaging system. The use of LYSO crystals, with their relatively high density, has been proposed for prompt gamma imaging. However, very few LYSO Compton camera prototypes, let alone those combined with PET systems, have been built and evaluated in practice. We developed a prototype that comprises two existing detectors that use LYSO-SiPM in our laboratory. These detectors were mounted on a rotational stage, thus enabling them to function either as a Compton camera or as a PET detector pair. Distinct energy windows were employed to differentiate Compton events from PET events. The encoding circuit feeds the 64-channel signals from each SiPM into a capacitive multiplexing circuit, which reduces the number of signals from 64 to 4

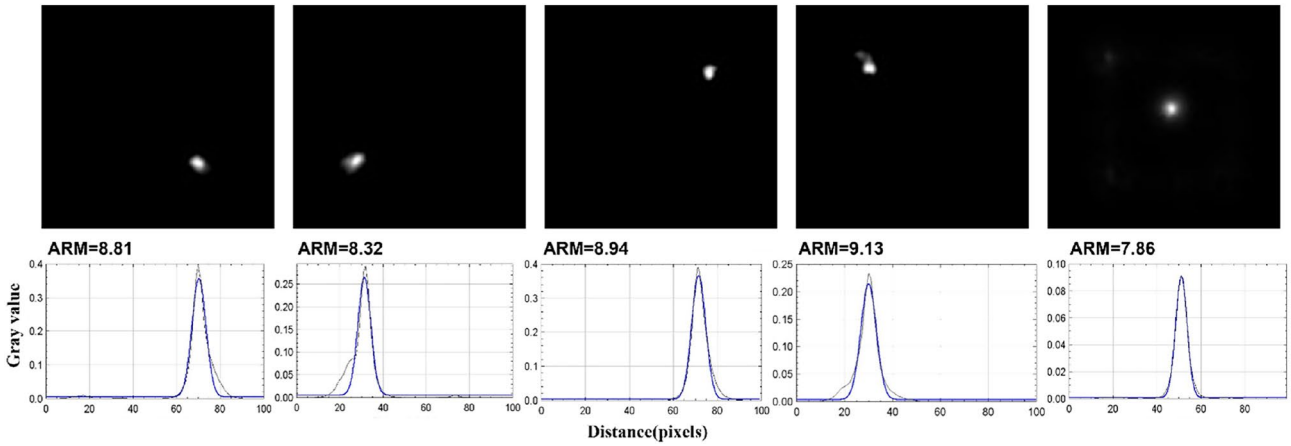

Fig. 16 (Color online) Experimental Compton images obtained in Compton imaging mode and the ARM distribution of a ^{60}Co source at 5 positions via the MLEM

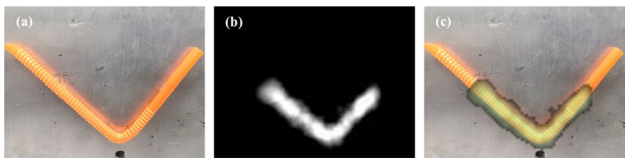

Fig. 17 (Color online) **a** V-shaped phantom made from tubing filled with ^{18}F. **b** Experimental Compton image obtained in Compton imaging mode of the V-shaped phantom. **c** Fused image of (**a**) and (**b**)

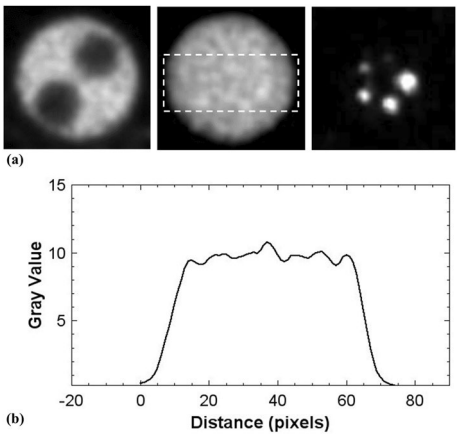

Fig. 18 (Color online) **a** Experimental results for the small animal NEMA phantom for the cold region, uniform region and rod region, which ranged from 1 to 5 mm in diameter, in the PET imaging mode and **b** line profile of the uniform region in the white dashed rectangular region

position-weighted outputs. This approach is used to decode the 50×50 dense-pixel LYSO detectors, thereby significantly simplifying the data processing procedure.

Monte Carlo simulations, as well as experimental validations, were conducted separately for the system operating

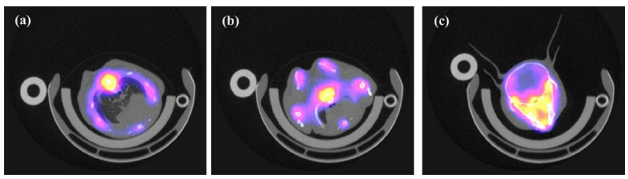

Fig. 19 (Color online) Mouse imaging results for the **a** rib, **b** arm and **c** head obtained in PET imaging mode; PET and CT images were manually registered and superimposed

in both Compton imaging mode and PET imaging mode. In addition to point source imaging studies for performance evaluation, the feasibility of phantom imaging in Compton imaging mode by imaging a V-shaped distribution source was successfully demonstrated. Furthermore, a mouse imaging experiment in PET imaging mode was carried out, which revealed the potential for application of the Compton/PET hybrid imaging system in small animal models.

Our observations revealed remarkable performance of the prototype hybrid system in both Compton imaging mode and PET imaging mode. Further enhancements to the overall system's image resolution and/or sensitivity would entail optimizing the detector design, which typically involves a trade-off between the desired performance and cost-effectiveness, constrained by factors such as mechanical integration and image correction techniques. The angular resolution of a Compton camera is influenced by factors such as the energy resolution of the detectors; geometric effects such as the intrinsic detector spatial resolution and scatterer-to-absorber distance; and the Doppler effect. In this study, both detectors were LYSO scintillation detectors. Employing semiconductor detectors, such as silicon detectors, could yield higher energy resolution and, consequently, improved angular resolution, albeit at a higher cost.

Decisions regarding the crystal dimensions of the detectors also hinge on balancing detection sensitivity and system resolution. A shorter crystal length can mitigate the parallax effect for PET imaging and decrease the geometric contribution to angular resolution for Compton imaging at the expense of sensitivity degradation. Conversely, a larger crystal section can enhance the overall system sensitivity by increasing the solid angle coverage, albeit at the cost of resolution degradation. Thus, careful consideration of various factors is imperative for optimizing detector design before a hybrid system is implemented. Compared with previously developed systems [51, 52], we used a small-pixel, large-array LYSO detector as the scatterer layer (with a pixel size of 0.9 mm × 0.9 mm and an array size of 50 mm × 50 mm), which improved the sensitivity of the Compton camera and significantly reduced the influence of geometric factors on the spatial resolution. For future commercial devices, further studies are needed to ascertain the most cost-effective design for the proposed Compton/PET hybrid imaging technology.

In this study, the data acquisition (DAQ) system used a 50 million samples per second (MSPS) analog-to-digital converter (ADC), which resulted in a timestamp unit of 20 ns. Consequently, the minimum coincidence time window that could be set in the experiment was 20 ns, and the time difference for all coincidence events was also 20 ns. Employing faster DAQ would enable the use of a narrower time window, thereby aiding in the reduction of random coincidences.

The hybrid imaging system introduced in this study was constructed with two preexisting detectors available in the laboratory. Owing to the limited number of detectors, the two imaging modalities, Compton imaging and positron emission tomography (PET) imaging, were implemented separately. Similarly, in PET imaging mode, only coincidence events between the two detectors can be captured. However, with the implementation of a two-ring system, additional scatterer–absorber and absorber–absorber coincidence events can be obtained, thus augmenting the total number of useful events. These supplementary events hold potential for enhancing the image signal-to-noise ratio through improved image reconstruction techniques.

In our prototype system, the two detectors employed crystals with different dimensions, which resulted in an asymmetric geometry for the collected PET data. To accommodate this unconventional setup, we developed a general-purpose PET reconstruction framework capable of reconstructing images under arbitrary spatial placements of detector crystals with varying dimensions, thereby supporting the asymmetric geometry of our Compton/PET hybrid imaging system. Image reconstruction software was devised on the basis of a list-mode MLEM algorithm run on multiple GPUs, thereby enabling real-time computation of the system matrix. Attenuation correction was implemented via forward projection of the attenuation coefficient map derived from the known object geometry, typically obtained from computed tomography (CT) images. This correction accounts for attenuation effects within both the imaging objects and the detectors, which is particularly relevant if a two-ring system is to be constructed. The normalization step in the software simplifies the process by considering only geometric effects and individual crystal efficiency. To obtain fully quantitative PET images from the Compton/PET hybrid imaging system, future iterations of the reconstruction software should incorporate additional factors such as dead time parameters, detector interference patterns and axial effects. Scatter and random corrections are imperative for accurate image reconstruction. By incorporating scatter and random corrections, the final images can more accurately represent the true distribution of radiotracer uptake in the imaged object, thereby bolstering the reliability and diagnostic efficacy of the imaging system.

Additionally, reconstruction for Compton scattering events was conducted via rapid reconstruction software based on the list-mode MLEM algorithm, which was optimized for parallel execution across multiple GPUs. The system matrix was derived via Geant4 simulations, which involved systematically scanning a point source throughout the imaging volume and capturing the system's sensitivity in Compton imaging mode.

5 Conclusion

In this study, we introduced a LYSO-SiPM-based Compton/PET hybrid imaging system and developed a prototype to assess its feasibility and performance through simulation and experimentation. The simulation results demonstrate the system's ability to conduct Compton and PET imaging. Point source simulations revealed a 7.8° angular resolution (FWHM) for Compton imaging and the ability to discern tumors as small as 1 mm in diameter in PET imaging mode. Additionally, phantom imaging and mouse imaging experiments were conducted. In Compton imaging mode, the prototype accurately imaged point sources at various positions, whereas in PET imaging mode, it successfully identified tumors with a diameter of 1 mm. The PET imaging capabilities were further validated in mouse imaging experiments, where the obtained PET images corresponded well to CT images from a commercial PET/CT system.

Notably, scatter correction and random correction were not integrated into the PET image reconstruction during this preliminary evaluation, and these aspects will be addressed in future studies. In this study, we focused on constructing a simple prototype from existing detectors from our laboratory and evaluating two distinct imaging modes, namely, Compton imaging and PET imaging, with the same detectors. Moving forward, we aim to develop

a full-ring Compton/PET hybrid imaging system and explore various coincidence data and imaging modes, as well as combinations of modes. Future work will also concentrate on integrating PET and Compton imaging into a single scan and achieving simultaneous imaging of multiple energy sources.

Acknowledgements The authors would like to thank Yi-Ming Chen and Qing Ruan for providing the radiopharmaceuticals and the conditions for the mouse imaging experiments.

Author Contributions All authors contributed to the study conception and design. Material preparation, data collection and analysis were performed by Hai-Hao Wang, Yu-Cun Hou, Jian-Lang Hua, Zi-Quan Yuan, Chen-Xi Li, Run-Ze Liao and Jian-Yong Jiang. The first draft of the manuscript was written by Hai-Hao Wang and all authors commented on previous versions of the manuscript. All authors read and approved the final manuscript.

Data Availability The data that support the findings of this study are openly available in Science Data Bank at https://cstr.cn/31253.11.sciencedb.j00186.00808 and https://doi.org/10.57760/sciencedb.j00186.00808.

Declarations

Conflict of interest The authors declare that they have no Conflict of interest.

References

1. P. Som, H.L. Atkins, D. Bandoypadhyay et al., A fluorinated glucose analog, 2-fluoro-2-deoxy-D-glucose (F-18): nontoxic tracer for rapid tumor detection. J. Nucl. Med. **21**, 670–675 (1980)
2. Z.Q. Chen, Y.L. YE, L.I. Chen et al., Investigation of pet imaging experiment and monte carlo simulation for cancer therapy using heavy-ion beams at HIRFL. Chin. Phys. C **28**, 792–796 (2004) http://hepnp.ihep.ac.cn/en/article/id/6bdc71e7-69e9-4c1b-acf7-3be914412e85
3. T.K. Lewellen, Recent developments in PET detector technology. Phys. Med. Biol. **53**, R287 (2008). https://doi.org/10.1088/0031-9155/53/17/R01
4. Y.Y. Lu, J.H. Chen, J.A. Liang et al., Clinical value of FDG PET or PET/CT in urinary bladder cancer: a systemic review and meta-analysis. Eur. J. Radiol. **81**, 2411–2416 (2012). https://doi.org/10.1016/j.ejrad.2011.07.018
5. R. Sadeghi, S.R. Zakavi, M. Hasanzadeh et al., Diagnostic performance of fluorine-18-fluorodeoxyglucose positron emission tomography imaging in uterine sarcomas: systematic review and meta-analysis of the literature. Int. J. Gynecol. Cancer **23**, 1349–1356 (2013). https://doi.org/10.1097/IGC.0b013e3182a20e18
6. E. Berg, S.R. Cherry, Innovations in instrumentation for positron emission tomography. Semin. Nucl. Med. **48**(4), 311–331 (2018). https://doi.org/10.1053/j.semnuclmed.2018.02.006
7. J.L. Vercher-Conejero, L. Pelegrí-Martinez, D. Lopez-Aznar et al., Positron emission tomography in breast cancer. Diagnostics **5**, 61–83 (2015). https://doi.org/10.3390/diagnostics5010061
8. K. Paydary, S.M. Seraj, M.Z. Zadeh et al., The evolving role of FDG-PET/CT in the diagnosis, staging, and treatment of breast cancer. Mol. Imaging Biol. **21**, 1–10 (2019). https://doi.org/10.1007/s11307-018-1181-3
9. M.E. Juweid, B.D. Cheson, Positron-emission tomography and assessment of cancer therapy. N. Engl. J. Med. **354**, 496–507 (2006). https://doi.org/10.1056/NEJMra050276
10. J. Czernin, M. Allen-Auerbach, R.H. Schelbert et al., Improvements in cancer staging with PET/CT: literature-based evidence as of September 2006. J. Nucl. Med. **48**, 78S-88S (2007)
11. N.I. Bohnen, D.S.W. Djang, K. Herholz et al., Effectiveness and safety of ^{18}F-FDG PET in the evaluation of dementia: a review of the recent literature. J. Nucl. Med. **53**, 59–71 (2012). https://doi.org/10.2967/jnumed.111.096578
12. C. Marcus, E. Mena, R.M. Subramaniam, Brain PET in the diagnosis of Alzheimer's disease. Clin. Nucl. Med. **39**, e413–e426 (2014). https://doi.org/10.1097/RLU.0000000000000547
13. S. Wei, N. Joshi, M. Salerno et al., PET imaging of leg arteries for determining the input function in PET/MRI brain studies using a compact, MRI-compatible PET system. IEEE Trans. Radiat. Plasma Med. Sci. **6**, 583–591 (2021). https://doi.org/10.1109/trpms.2021.3111841
14. S.K. Royse, B.J. Lopresti, C.A. Mathis et al., Beyond monoamines: II. Novel applications for PET imaging in psychiatric disorders. J. Neurochem. **164**, 401–443 (2023). https://doi.org/10.1111/jnc.15657
15. L. Zhang, T. Xie, K. Zhou et al., in *JOURNAL OF LABELLED COMPOUNDS & RADIOPHARMACEUTICALS*, F-18-labeled styrylquinoxaline derivatives as tau probes for PET. Vol. 62, WILEY 111 RIVER ST, HOBOKEN 07030-5774, NJ USA, pp. S413–S414 (2019)
16. M. Cui, X. Wang, P. Yu et al., Synthesis and evaluation of novel ^{18}F labeled 2-pyridinylbenzoxazole and 2-pyridinylbenzothiazole derivatives as ligands for positron emission tomography (PET) imaging of β-amyloid plaques. J. Med. Chem. **55**, 9283–9296 (2012). https://doi.org/10.1021/jm300973k
17. M. Cui, M. Ono, H. Kimura et al., Radioiodinated benzimidazole derivatives as single photon emission computed tomography probes for imaging of β-amyloid plaques in Alzheimer's disease. Nucl. Med. Biol. **38**, 313–320 (2011). https://doi.org/10.1016/j.nucmedbio.2010.09.012
18. Y. Yang, M. Cui, B. Jin et al., 99mTc-labeled dibenzylideneacetone derivatives as potential SPECT probes for in vivo imaging of β-amyloid plaque. Eur. J. Med. Chem. **64**, 90–98 (2013). https://doi.org/10.1016/j.ejmech.2013.03.057
19. X. Chen, M.-C. Cui, W. Deuther-Conrad et al., Synthesis and biological evaluation of a novel ^{99m}Tc cyclopentadienyl tricarbonyl complex ([(Cp-R)^{99m}Tc (CO)$_3$]) for sigma-2 receptor tumor imaging. Bioorg. Med. Chem. Lett. **22**, 6352–6357 (2012). https://doi.org/10.1016/j.bmcl.2012.08.083
20. S.R. Cherry, J.A. Sorenson, M.E. Phelps et al., *Physics in nuclear medicine*, (Soc Nuclear Med, 2013)
21. F.F. Alqahtani, SPECT/CT and PET/CT, related radiopharmaceuticals, and areas of application and comparison. Saudi Pharm. J. **31**, 312–328 (2023). https://doi.org/10.1016/j.jsps.2022.12.013
22. T. Ma, R. Yao, Y. Shao, Determination of geometrical parameters for slit-slat SPECT imaging on MicroPET. 2007 IEEE Nuclear Science Symposium Conference Record, Honolulu, HI, USA, 2007, pp. 4285-4288. https://doi.org/10.1109/NSSMIC.2007.4437063
23. T.T. Dai, T. Ma, H. Liu et al., A high-resolution small animal SPECT system developed at Tsinghua. Nucl. Sci. Tech. **22**, 344–348 (2011). https://doi.org/10.13538/j.1001-8042/nst.22.344-348
24. T. Ma, T. Xu, H. Liu et al., Development of a SiPM based preclinical PET SPECT imaging system imaging system. J. Nucl. Med. **58**, 397–397 (2017). https://jnm.snmjournals.org/content/58/supplement_1/397
25. M. Dahlbom, L.R. MacDonald, M. Schmand et al., A YSO/LSO phoswich array detector for single and coincidence photon

imaging. IEEE Trans. Nucl. Sci. **45**, 1128–1132 (1998). https://doi.org/10.1109/23.681990
26. A. Del Guerra, C. Damiani, G. Di Domenico et al., An integrated PET-SPECT small animal imager: preliminary results. IEEE Trans. Nucl. Sci. **47**, 1537–1540 (2000). https://doi.org/10.1109/23.873012
27. P. Guerra, J.L. Rubio, J.E. Ortuno et al., Performance analysis of a low-cost small animal PET/SPECT scanner. Nucl. Instrum. Methods Phys. Res. Sect. A **571**, 98–101 (2007). https://doi.org/10.1016/j.nima.2006.10.038
28. Y. Shao, R. Yao, T. Ma et al., Initial studies of PET-SPECT dual-tracer imaging. 2007 IEEE Nuclear Science Symposium Conference Record, Honolulu, HI, USA, 2007, pp. 4198-4204. https://doi.org/10.1109/NSSMIC.2007.4437043
29. M.C. Goorden, F. van der Have, R. Kreuger et al., VECTor: a preclinical imaging system for simultaneous submillimeter SPECT and PET. J. Nucl. Med. **54**, 306–312 (2013). https://doi.org/10.2967/jnumed.112.109538
30. P. Fan, B.F. Hutton, M. Holstensson et al., Scatter and crosstalk corrections for ^{99m}Tc/^{123}I dual-radionuclide imaging using a CZT SPECT system with pinhole collimators. Med. Phys. **42**, 6895–6911 (2015). https://doi.org/10.1118/1.4934830
31. S. Iwano, K. Kato, S. Ito et al., FDG-PET performed concurrently with initial I-131 ablation for differentiated thyroid cancer. Ann. Nucl. Med. **26**, 207–213 (2012). https://doi.org/10.1007/s12149-011-0559-y
32. A.M. Avram, Radioiodine scintigraphy with SPECT/CT: an important diagnostic tool for thyroid cancer staging and risk stratification. J. Nucl. Med. Technol. **42**, 170–180 (2014). https://doi.org/10.2967/jnumed.111.104133
33. B.R. Haugen, 2015 American Thyroid Association management guidelines for adult patients with thyroid nodules and differentiated thyroid cancer: what is new and what has changed? Cancer **123**, 372–381 (2017). https://doi.org/10.1002/cncr.30360
34. U. Feine, R. Lietzenmayer, J.-P. Hanke et al., Fluorine-18-FDG and iodine-131-iodide uptake in thyroid cancer. J. Nucl. Med. **37**, 1468–1472 (1996). https://jnm.snmjournals.org/content/37/9/1468
35. J.S. Yeo, J. Chung, Y. So et al., F-18-fluorodeoxyglucose positron emission tomography as a presurgical evaluation modality for I-131 scan-negative thyroid carcinoma patients with local recurrence in cervical lymph nodes. Head Neck-J Sci. Spec. **23**, 94–103 (2001). https://doi.org/10.1002/1097-0347(200102)23
36. R. Caetano, C.R.G. Bastos, I.A.G. de Oliveira et al., Accuracy of positron emission tomography and positron emission tomography-CT in the detection of differentiated thyroid cancer recurrence with negative ^{131}I whole-body scan results: a meta-analysis. Head Neck **38**, 316–327 (2016). https://doi.org/10.1097/MNM.0b013e32832dcfa7
37. K. Ogane, M. Uenomachi, K. Shimazoe et al., Simultaneous measurements of single gamma ray of ^{131}I and annihilation radiation of ^{18}F with Compton PET hybrid camera. Appl. Radiat. Isot. **176**, 109864 (2021). https://doi.org/10.1016/j.apradiso.2021.109864
38. P. Fan, B.F. Hutton, M. Holstensson et al., Scatter and crosstalk corrections for ^{99m}Tc/^{123}I dual-radionuclide imaging using a CZT SPECT system with pinhole collimators. Med. Phys. **42**, 6895–6911 (2015). https://doi.org/10.1118/1.4934830
39. V. Schönfelder, A. Hirner, K. Schneider, A telescope for soft gamma ray astronomy. Nucl. Instru. Meth. **107**, 385–394 (1973). https://doi.org/10.1016/0029-554X(73)90257-7
40. K. Parodi, On-and off-line monitoring of ion beam treatment. Nucl. Instrum. Methods Phys. Res. Sect. A **809**, 113–119 (2016). https://doi.org/10.1016/j.nima.2015.06.056
41. Z. He, W. Li, G.F. Knoll et al., 3-D position sensitive CdZnTe gamma-ray spectrometers. Nucl. Instrum. Methods Phys. Res. Sect. A **422**, 173–178 (1999). https://doi.org/10.1016/S0168-9002(99)00841-4
42. Y.F. Du, Z. He, G.F. Knoll et al., Evaluation of a Compton scattering camera using 3-D position sensitive CdZnTe detectors. Nucl. Instrum. Methods Phys. Res. Sect. A **457**, 203–211 (2001). https://doi.org/10.1016/S0168-9002(00)00669-0
43. J. Jiang, K. Shimazoe, Y. Nakamura et al., A prototype of aerial radiation monitoring system using an unmanned helicopter mounting a GAGG scintillator Compton camera. J. Nucl. Sci. Technol. **53**, 1067–1075 (2016)
44. S. Motomura, S. Enomoto, H. Haba et al., Gamma-ray Compton imaging of multitracer in biological samples using strip germanium telescope. IEEE Trans. Nucl. Sci. **54**, 710–717 (2007). https://doi.org/10.1109/TNS.2007.894209
45. F.T. Tanimori, H. Amano, K. Hattori et al., Development of Electron tracking Compton Camera based on micro pixel gas detector and its application for medical imaging. in 2008 IEEE Nuclear Science Symposium Conference Record, 616–620 (2008). https://doi.org/10.1109/NSSMIC.2008.4774081
46. S. Takeda, H. Odaka, S. Ishikawa et al., Demonstration of in-vivo multi-probe tracker based on a Si/CdTe semiconductor Compton camera. IEEE Trans. Nucl. Sci. **59**, 70–76 (2012). https://doi.org/10.1109/TNS.2011.2178432
47. Y.F. Yang, Y. Gono, S. Motomura et al., A Compton camera for multitracer imaging. IEEE Trans. Nucl. Sci. **48**, 656–661 (2001). https://doi.org/10.1109/23.940142
48. Y. Suzuki, M. Yamaguchi, H. Odaka et al., Three-dimensional and multienergy gamma-ray simultaneous imaging by using a Si/CdTe Compton camera. Radiology **267**, 941–947 (2013). https://doi.org/10.1148/radiol.13121194
49. T. Lee, H. Lee, W. Lee et al., Monitoring the distribution of prompt gamma rays in boron neutron capture therapy using a multiple-scattering Compton camera: A Monte Carlo simulation study. Nucl. Instrum. Methods Phys. Res. Sect. A **798**, 135–139 (2015). https://doi.org/10.1016/j.nima.2015.07.038
50. K. Shimazoe, M. Yoshino, Y. Ohshima et al., Development of simultaneous PET and Compton imaging using GAGG-SiPM based pixel detectors. Nucl. Instrum. Methods Phys. Res. Sect. A **954**, 161499 (2020). https://doi.org/10.1016/j.nima.2018.10.177
51. E. Yoshida, H. Tashima, K. Nagatsu et al., Whole gamma imaging: a new concept of PET combined with Compton imaging. Phys. Med. Biol. **65**, 125013 (2020). https://doi.org/10.1088/1361-6560/ab8e89
52. K. Ogane, M. Uenomachi, K. Shimazoe et al., Simultaneous measurements of single gamma ray of ^{131}I and annihilation radiation of ^{18}F with Compton PET hybrid camera. Appl. Radiat. Isot. **176**, 109864 (2021). https://doi.org/10.1016/j.apradiso.2021.109864
53. G. Llosá, M. Rafecas, Hybrid PET/Compton-camera imaging: an imager for the next generation. Eur. Phys. J. Plus **138**, 214 (2023). https://doi.org/10.1140/epjp/s13360-023-03805-9
54. V. Ilisie, V. Giménez-Alventosa, L. Moliner et al., Building blocks of a multi-layer PET with time sequence photon interaction discrimination and double Compton camera. Nucl. Instrum. Methods Phys. Res. Sect. A **895**, 74–83 (2018). https://doi.org/10.1016/j.nima.2018.03.076
55. K.A. Comanor, P.R.G. Virador, W.W. Moses, Algorithms to identify detector compton scatter in PET modules. IEEE Trans. Nucl. Sci. **43**, 2213–2218 (1996). https://doi.org/10.1109/23.531884
56. M. Rafecas, G. Böning, B.J. Pichler et al., Inter-crystal scatter in a dual layer, high resolution LSO-APD positron emission tomograph. Phys. Med. Biol. **48**, 821 (2003). https://doi.org/10.1088/0031-9155/48/7/302
57. C. Lang, D. Habs, K. Parodi et al., Sub-millimeter nuclear medical imaging with high sensitivity in positron emission tomography using $\beta+\gamma$ coincidences. J. Instrum. **9**, P01008 (2014). https://doi.org/10.1088/1748-0221/9/01/P01008

58. J. Barrio, N. Cucarella, A.J. Gonzalez et al., Characterization of a high-aspect ratio detector with lateral sides readout for compton PET. IEEE Trans. Radiat. Plasma Med. Sci. **4**, 546–554 (2020). https://doi.org/10.1109/TRPMS.2020.3006862
59. T. Yamaya, E. Yoshida, H. Tashima et al., Whole gamma imaging (WGI) concept: simulation study of triple-gamma imaging. J. Nucl. Med. **58**, 152–152 (2017). https://jnm.snmjournals.org/content/58/supplement_1/152
60. T. Yamaya, E. Yoshida, H. Tashima et al., Concrete realization of the whole gamma imaging concept. IEEE Nuclear Science Symposium and Medical Imaging Conference (NSS/MIC) Atlanta, GA, USA, 2017, pp. 1-3. https://doi.org/10.1109/NSSMIC.2017.8532867
61. H. Tashima, E. Yoshida, H. Wakizaka et al., 3D Compton image reconstruction method for whole gamma imaging. Phys. Med. Biol. **65**, 225038 (2020). https://doi.org/10.1016/j.apradiso.2021.109864
62. M. Sitarz, J.P. Cussonneau, T. Matulewicz et al., Radionuclide candidates for $\beta+\gamma$ coincidence PET: an overview. Appl. Radiat. Isot. **155**, 108898 (2020). https://doi.org/10.1016/j.apradiso.2019.108898
63. T. Matulewicz, Radioactive nuclei for $\beta+\gamma$ PET and theranostics: selected candidates. Bio-Algorithms Med-Syst. **17**, 235–239 (2022). https://doi.org/10.1515/bams-2021-0142
64. S.J. Park, W.L. Rogers, S. Huh et al., Performance evaluation of a very high resolution small animal PET imager using silicon scatter detectors. Phys. Med. Biol. **52**, 2807 (2007). https://doi.org/10.1088/0031-9155/52/10/012
65. P. Moskal, E. Stępień, Prospects and clinical perspectives of total-body PET imaging using plastic scintillators. PET Clin. **15**, 439–452 (2020). https://doi.org/10.1016/j.cpet.2020.06.009
66. S.C. Huang, R.E. Carson, E.J. Hoffman et al., An investigation of a double-tracer technique for positron computerized tomography. J. Nucl. Med. **23**, 816–822 (1982). https://jnm.snmjournals.org/content/23/9/816
67. K.J. Kearfott, Feasibility of simultaneous and sequentially administered dual tracer protocols for measurement of regional cerebral haematocrit using positron emission tomography. Phys. Med. Biol. **35**, 249 (1990). https://doi.org/10.1088/0031-9155/35/2/005
68. R.A. Koeppe, E.P. Ficaro, D.M. Raffel et al., CHAPTER 54-Temporally overlapping dual-tracer PET studies. Quantitative functional brain imaging with positron emission tomography. 359–366 (1998). https://doi.org/10.1016/B978-012161340-2/50056-1
69. J. Verhaeghe, Y. D'Asseler, S. Staelens et al., Noise properties of simultaneous dual tracer PET imaging. in IEEE Nuclear Science Symposium Conference Record, 2005, Vol. 5, pp. 2611–2614 (2005). https://doi.org/10.1109/NSSMIC.2005.1596873
70. F.P. Figueiras, X. Jiménez, D. Pareto et al., Simultaneous dual-tracer PET imaging of the rat brain and its application in the study of cerebral ischemia. Mol. Imaging Biol. **13**, 500–510 (2011). https://doi.org/10.1007/s11307-010-0370-5
71. D.J. Kadrmas, J.M. Hoffman, Methodology for quantitative rapid multi-tracer PET tumor characterizations. Theranostics **3**, 757 (2013). https://doi.org/10.7150/thno.5201
72. D.J. Kadrmas, T.C. Rust, Feasibility of rapid multitracer PET tumor imaging. IEEE Trans. Nucl. Sci. **52**, 1341–1347 (2005). https://doi.org/10.1109/TNS.2005.858230
73. A. Gajos, D. Kaminska, P. Moskal et al., Method for reconstructing multi-tracer metabolic and morphometric images and tomography system for multi-tracer metabolic and morphometric imaging., uS Patent 10,339,676 (Jul. 2 2019)
74. K.G. Tournoy, S. Maddens, R. Gosselin et al., Integrated FDG-PET/CT does not make invasive staging of the intrathoracic lymph nodes in non-small cell lung cancer redundant: a prospective study. Thorax **62**, 696–701 (2007). https://doi.org/10.1136/thx.2006.072959
75. K.J. Nichols, F.P. DiFilippo, C.J. Palestro, Computational approaches to detect small lesions in 18F-FDG PET/CT scans. J. Appl. Clin. Med. Phys. **22**, 125–139 (2021). https://doi.org/10.1002/acm2.13451
76. W. van der Bruggen, C.P. Bleeker-Rovers, O.C. Boerman et al., PET and SPECT in osteomyelitis and prosthetic bone and joint infections: a systematic review. Seminars Nucl. Med. **40**, 3–15 (2010). https://doi.org/10.1053/j.semnuclmed.2009.08.005
77. S.I. Heiba, D. Kolker, B. Mocherla et al., The optimized evaluation of diabetic foot infection by dual isotope SPECT/CT imaging protocol. J. Foot Ankle Surg. **49**, 529–536 (2010). https://doi.org/10.1053/j.jfas.2010.07.010
78. N.M. Hijnen, A. de Vries, K. Nicolay et al., Dual-isotope ^{111}In/^{177}Lu SPECT imaging as a tool in molecular imaging tracer design. Contrast Media Mol. Imaging **7**, 214–222 (2012). https://doi.org/10.1002/cmmi.485
79. B.L. Oliveira, F. Blasi, T.A. Rietz et al., Multimodal molecular imaging reveals high target uptake and specificity of 111In-and 68Ga-labeled fibrin-binding probes for thrombus detection in rats. J. Nucl. Med. **56**, 1587–1592 (2015). https://doi.org/10.2967/jnumed.115.160754
80. Z. Yao, Y. Xiao, M. Dong et al., Development of a two-layer dense-pixel LYSO Compton camera prototype for prompt gamma imaging. Phys. Med. Biol. **68**, 045008 (2023). https://doi.org/10.1088/1361-6560/acb4d8
81. S. Agostinelli, J. Allison, K. Amako et al., GEANT4-a simulation toolkit. Nucl. Instrum. Methods Phys. Res. Sect. A **506**, 250–303 (2003). https://doi.org/10.1016/S0168-9002(03)01368-8
82. S.J. Wilderman, N.H. Clinthorne, J.A. Fessler et al., List-mode maximum likelihood reconstruction of Compton scatter camera images in nuclear medicine. 1998 IEEE Nuclear Science Symposium and Medical Imaging Conference (Cat. No.98CH36255), Toronto, ON, Canada, 1998, pp. 1716–1720. https://doi.org/10.1109/NSSMIC.1998.773871
83. A.J. Mathews, K. Li, S. Komarov et al., A generalized reconstruction framework for unconventional PET systems. Med. Phys. **42**, 4591–4609 (2015). https://doi.org/10.1118/1.4923180
84. L. Parra, H.H. Barrett, List-mode likelihood: EM algorithm and image quality estimation demonstrated on 2-D PET. IEEE Trans. Med. Imaging **17**, 228–235 (1998). https://doi.org/10.1109/42.700734
85. J. Jiang, K. Li, S. Komarov et al., Feasibility study of a point-of-care positron emission tomography system with interactive imaging capability. Med. Phys. **46**, 1798–1813 (2019). https://doi.org/10.1002/mp.13397
86. G. Pratx, G. Chinn, P.D. Olcott et al., Fast, accurate and shift-varying line projections for iterative reconstruction using the GPU. IEEE Trans. Med. Imaging **28**, 435–445 (2008). https://doi.org/10.1109/TMI.2008.2006518
87. J. Cui, G. Pratx, S. Prevrhal et al., Fully 3D list-mode time-of-flight PET image reconstruction on GPUs using CUDA. Med. Phys. **38**, 6775–6786 (2011). https://doi.org/10.1118/1.3661998
88. H. Alva-Sánchez, A. Zepeda-Barrios, V.D. Díaz-Martínez et al., Understanding the intrinsic radioactivity energy spectrum from ^{176}Lu in LYSO/LSO scintillation crystals. Sci. Rep. **8**, 17310 (2018). https://doi.org/10.1038/s41598-018-35684-x
89. H. Alva-Sánchez, Background energy spectra for LSO/LYSO scintillation crystals of different geometries. J. Appl. Phys. **131**, 144501 (2022). https://doi.org/10.1063/5.0078453

Springer Nature or its licensor (e.g. a society or other partner) holds exclusive rights to this article under a publishing agreement with the author(s) or other rightsholder(s); author self-archiving of the accepted manuscript version of this article is solely governed by the terms of such publishing agreement and applicable law.